Research Square

Preprints are preliminary reports that have not undergone peer review.
They should not be considered conclusive, used to inform clinical practice,
or referenced by the media as validated information.

Shear force mixing versus ultrasonication of solution-processing carbon nanotubes for field-effect transistor applications

Debjani Goswami
Aston University
Petro Lutsyk
p.lutsyk@aston.ac.uk

Aston University

Research Article

Keywords: carbon nanotubes, shear force, field-effect transistor, interface trap density

Posted Date: July 23rd, 2026

DOI: https://doi.org/10.21203/rs.3.rs-10356276/v1

License: This work is licensed under a Creative Commons Attribution 4.0 International License.
Read Full License

Additional Declarations: No competing interests reported.

Shear force mixing versus ultrasonication of solution-processing carbon nanotubes for field-effect transistor applications

Debjani Goswami, Petro Lutsyk
Aston Institute of Photonic Technologies, School of Engineering and Innovation, Aston University, Aston Triangle, B4 7ET, Birmingham, UK
Corresponding author e-mails: d.goswami@aston.ac.uk (D.G.), p.lutsyk@aston.ac.uk (P.L.)

Abstract
Despite the widespread use of ultrasonication for dispersing carbon nanotubes, the suitability and advantages of shear-force mixing dispersion method remain unexplored, particularly for field-effect transistor (FET) application. This study compares ultrasonication and shear force mixing for dispersing small- and large-diameter single-walled carbon nanotubes and examines how each method affects nanotube quality and FET performance. The results show that the carbon nanotubes dispersed by shear force mixing provides better FET performance due to lower subthreshold swing and consequently reduced interface trap density. Furthermore, spectral (absorption, photoluminescence, Raman) characterization evidences lower level of defects in shear force mixing nanotube dispersions comparing to ultrasonication-dispersed samples. Besides, shear force mixing results in higher variability of nanotube chiralities in the obtained dispersions. The outcome of this comparative study provides new insights into impact of dispersion methodology on carbon nanotube quality, particularly formation of defects, and confirm feasibility of shear force technique for carbon nanotube processing towards fabrication of transistors and other nanoelectronics applications.

Keywords
carbon nanotubes, shear force, field-effect transistor, interface trap density

Acknowledgements
For the purposes of open access, the authors have applied a Creative Commons Attribution (CC BY) license to any Author Accepted Manuscript (AAM) version arising from this submission.
P.L. acknowledges support from the Royal Society Research Grant (RGS\R2\192502).

Introduction

Carbon nanotubes have unique electronic [1,2], optical [2], and mechanical properties [3] due to their one-dimensional structure [4,5]. There are promising nanotube applications in the areas of nanoelectronics [6], photonics [4], optoelectronics [4,5], and so on [7]. For example, single-wall carbon nanotubes (SWNTs) have been integrated into the channel region of field-effect transistors (FETs), enabling the development of SWNT FETs. These devices offer the potential for superior switching performance, improved scalability, and reduced power consumption compared with conventional silicon-based transistors [8]. However due to strong Van der Waals forces between the nanotubes, they are inherently cohesive and tend to form tightly bound bundles, which induce SWNTs aggregation and limit their dispersibility in most solvents [9,10]. Such aggregation leads to agglomeration and sedimentation, preventing the formation of stable, uniform nanotube dispersions and one of the major challenges in solution processing of SWNTs for electronic applications [11]. Therefore, identifying and optimizing dispersion strategies that minimize structural damage while producing stable, homogeneous SWNT dispersions remains essential [12].

Although ultrasonication (US) is widely used to disperse SWNTs for FET fabrication, the implementation of shear-force mixing (SFM) solution processing of SWNTs in transistor devices remains largely underexplored. SFM method uses low-force mechanical shear to separate tube bundles and can be applied for large-scale dispersion of carbon nanotubes. In contrast, US can damage the tubes by breaking into shorter lengths and introduce defects into the nanotubes due to strong cavitation forces [13,14]. Furthermore, US is limited to small volume dispersion for research purposes and requires solid alternatives for industrial scale applications. Shea et al. demonstrated that photovoltaic devices made of (6,5) chirality SWNTs using SFM method are outperforming the devices made of US-processed nanotubes [13]. This outcome was supplemented by the nanotube length characterization, which showed that 20-hours SFM produced relatively long SWNTs (average length of 1.09 μm), whereas 1-hour US resulted in much shorter SWNTs (0.3 μm average length). Graf et al. compared several methods including SFM, bath US, tip US, and gel chromatography for dispersing SWNTs of (6,5) chirality [14]. The results showed that SFM produced the longest nanotubes (with average length of 1.82 μm). Optical characterization indicated that the SWNTs dispersed by SFM exhibited significantly higher photoluminescence quantum yield (PLQY), indicating better preservation of the electronic structure and fewer defects for SFM processing of the nanotubes compared to other techniques.

Overall, the state-of-the-art studies have demonstrated that SFM is a scalable and less destructive dispersion technique compared with US, providing high-quality SWNT dispersions suitable for photonic and photovoltaic device fabrication [13,14]. However, the SFM of SWNTs has not been explored for FET applications, which is one of the key areas of nanotube application [8]. In this paper, we systematically compare two widely used solution-processing techniques: US and SFM for both small diameter (average 0.78 nm; predominantly (6,5) chirality) and large diameter (ranging 1.2-1.7 nm) SWNTs, evaluating how each dispersion method impact FET performance. By directly comparing US and SFM processed SWNTs in FET devices, new insights can be gained on how dispersion methodology influences SWNT quality and the resulting electrical characteristics of SWNT-based transistors.

Experimental

1. Preparation of SWNT Dispersions

SWNTs (Sigma Aldrich / Merck) of small diameter [0.78 nm average diameter; predominantly (6,5) chirality] (SG65i CoMoCAT from SouthWest NanoTechnologies (SWeNT), now represented by CHASM Advanced Materials (Signis® brand)) and large diameter [in the range of 1.2 - 1.7 nm] (PureTubes™, NanoIntegris, Inc.) were used. To prepare the SWNT dispersions, poly[(9,9-dioctylfluorenyl-2,7-diyl)-alt-co-(6,6′-{2,2′-bipyridine})] (PFO-BPy) (American Dye Source Inc.) was used as a dispersing agent (Figure 1a). SWNT powder was dispersed in toluene solution of PFO-BPy with varied materials portions for dispersion optimization reasons. Table 1 summarizes the material portions and dispersion conditions used for small- and large diameter SWNTs processing by US and SFM. The table provides a direct comparison of nanotube mass, solvent volume, PFO-BPy concentration.

Table 1 The material portions (SWNT powder, PFO-BPy, solvent) used for SWNTs processing.

SWNT type	Processing method	SWNT powder mass, mg	Solvent volume, mL	PFO-BPy concentration, g/L
small diameter	US	3	10	2
	SFM	18	30	2
large diameter	US	5	10	1
	SFM	15	30	1

Tip US was performed by a UP400S ultrasonic processor (Hielscher Ultrasonics GmbH), with the pulse length being 75% and ultrasonic power at 60% of maximum. For SFM, L4RT high shear mixer (Silverson) was used with an Emulsor Screen (Silverson) at 10,200 rpm with room temperature sample cooling bath.

All SWNT dispersions were centrifuged using a MiniSpin Plus centrifuge (Eppendorf SE) at 14,000 rpm for 10 minutes. The upper 50% of the supernatants were collected to remove nanotube bundles and obtain purified semiconducting SWNT dispersions.

2. Spectral Characterization of SWNT Dispersions

The absorption spectra were measured with a double-beam Lambda 1050 UV/VIS/NIR spectrophotometer (Perkin Elmer). The photoluminescence (PL) spectra and excitation-emission photoluminescence maps (PLE maps) were measured by a NanoLog excitation–emission spectrofluorometer (Horiba). The spectrofluorometer is equipped with a silicon detector for visible range measurements and a liquid-nitrogen-cooled InGaAs array detector was used for NIR range. PLE maps plots PL intensity two-dimensionally, where the X-axis is the emission wavelength of PL (λ_{EM}) and the Y-axis is the excitation wavelength of PL (λ_{EX}). Raman spectra were measured with dual-channel automated Raman confocal microscope RAMOS S120 (Ostec Instruments) and taken from at least 3 quasi random points. For Raman characterization, SWNT dispersions were deposited onto SiO_2 wafers (same as FET substrates; Fraunhofer Institute for Photonic Microsystems, Dresden, Germany) via drop-casting method and then dried overnight.

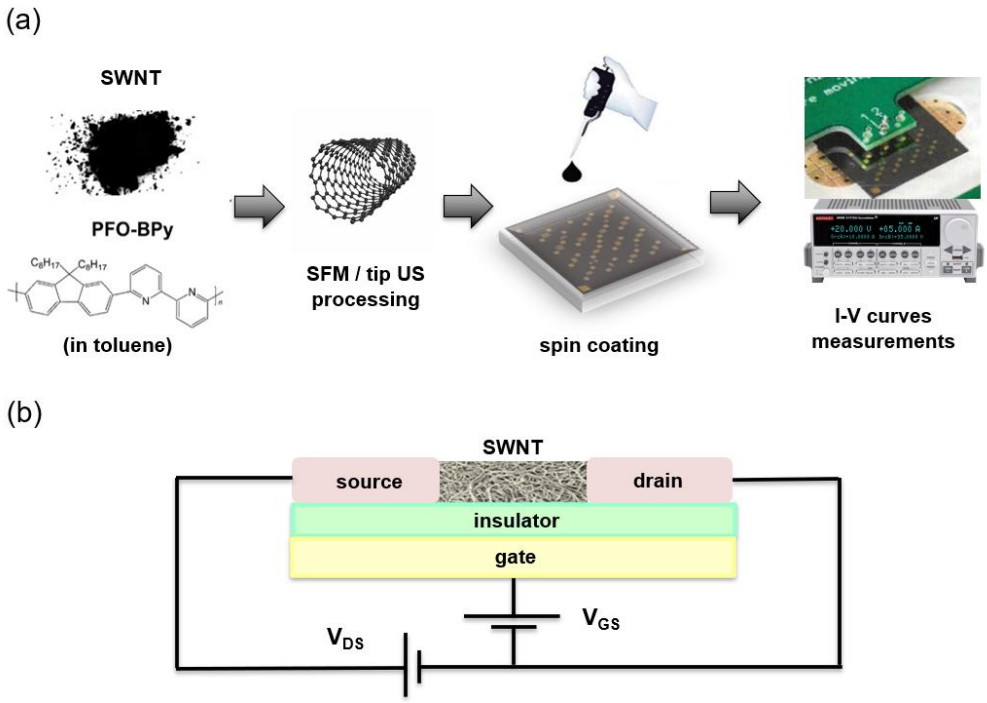


Fig. 1 (a) Schematic description of the procedures used to prepare nanotube samples. (b) Field effect transistor (FET) schematics with bottom gate and a network of SWNTs as a top semiconductor layer

3. Fabrication and Characterization of FETs

Silicon(n+)/SiO_2 wafers with deposited gold interdigital electrodes (Fraunhofer Institute for Photonic Microsystems, Dresden, Germany) were used as substrates to produce bottom-gate FET with SWNTs (Figure 1b). The SiO_2 layer is 90 nm thick, the length, L, and width of the FET channel, W, amounted to 2.5 μm and 1 cm, respectively. The surface capacitance of the insulator, C_i, was equal to 38.3 nF/cm^2. The substrates were cleaned in acetone with ultrasonication bath for 10 minutes followed by the annealing at 400°C in vacuum ((3-5)·10^{-6} Torr) for 20 minutes. Thin film of semiconductor SWNTs were deposited on the substrate by spin coating (10,000 rpm) followed by the annealing at 300°C for 20 minutes aiming to remove organic residuals.

Current-voltage FET characteristics were measured using a PC controlled dual-channel Keithley 2634B sourcemeter in ambient atmosphere. Before FET characterization of SWNT samples, controlled electrical breakdown technique [15] was applied aiming to remove residual metallic (highly conductive) nanotubes in the FET channel. The following process for electrical breakdown was used. At the constant gate-source voltage V_{GS} = +20 V, a relatively high drain-source voltage, V_{DS}, in the range of (10-19) V was applied, at which the electrical breakdown of the most conductive nanotubes occurs. I-V characteristics were analyzed on the following FET parameters: on-off current ratio, threshold voltage (V_T), charge carrier mobility, subthreshold swing (SS). To minimize hysteresis of transfer characteristics, the I-V curves were measured by changing V_{GS} from -40 to +5 V.

Results and Discussion

1. Optical Characterization

1.1 Absorption Spectra

The absorption spectra of studied SWNT dispersions are presented in Figure 2. The spectra are normalized by peak position of E_{11} transitions allowing us to visualize specific differences of the nanotubes obtained by US and SFM. Small diameter SWNTs (Figure 2a) have strong and narrow peaks featuring E_{11} (1001 nm for US, 999 nm for SFM) and E_{22} (573.5 nm for US, 573.0 nm for SFM) transitions for isolated nanotubes of the (6,5) chirality, respectively. The red-shifted peaks for US processed SWNTs of the (6,5) chirality can be associated with more defects [14] present in such samples comparing to SFM samples. Small spectral shoulder in the range of 1020-1050 nm for SFM sample (Figure 2a, curve 2) might be featuring E_{11} transitions for SWNTs of (7,5) chirality. To provide better understanding for E_{11} absorption spectral features, Gaussian fittings have been used in the range of E_{11} peak (900-1100nm; full details of the Gaussian parameters provided in supplementary Figure S1, Table S1). The fitting showed that the peak of (7,5) chirality (1030nm; 1.204-1.206 eV) is nearly twice as high for SFM treated SWNTs, evidencing higher content of this chirality in the dispersion.

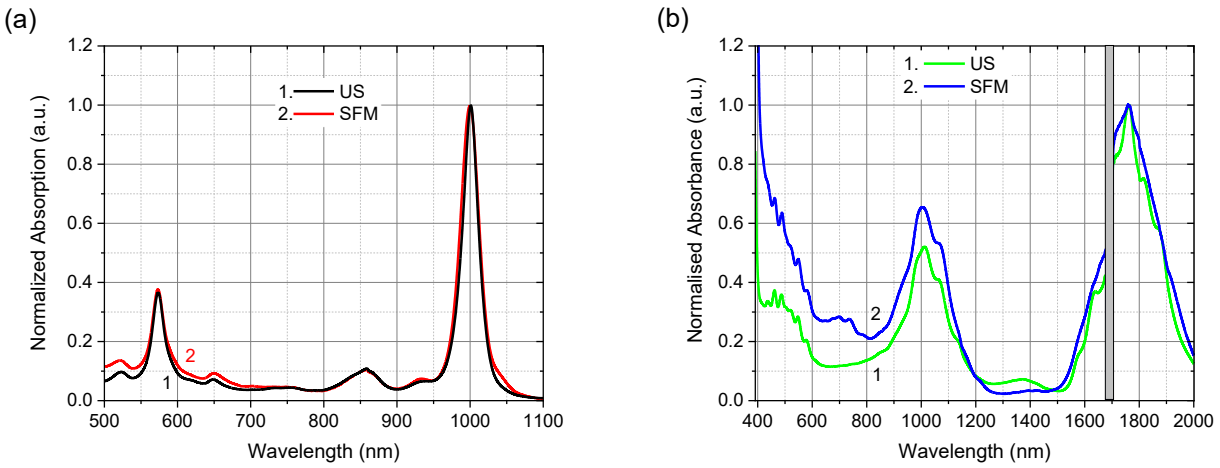


Fig. 2 Absorption spectra normalized by peak position of E_{11} transitions for small (a) and large (b) diameter SWNT dispersed by US (curves 1) and SFM (curves 2). (b) The greyed-out area in the range of 1675-1705 nm highlights the data range extracted from the spectra due to high intrinsic absorption of the toluene

The absorption spectra for large diameter SWNTs (Figure 2b) have the following characteristics: E_{11} maximum is at the 1763 nm for US and 1759 nm for SFM samples. The closest assignment for such sharp peak is (14,7) chirality (diameter 1.47 nm) [16]. E_{22} peak is positioned at 1011 nm and 1006 nm for US and SFM processed SWNT, respectively. There are several options for chirality assignment for such broad E_{22} band [16]. There is substantial red shift of E_{22} (Δ = 5 nm) and E_{11} peaks (Δ = 4 nm) for US treated nanotubes, evidencing higher levels of defects, as shown in small diameter SWNTs. There is additional broad peak at 1373 nm for US processed nanotubes that can be assigned to several chiralities according to [16], however this spectral signature has no PL

signal in this range, therefore it is most likely originating from non-semiconductor nanotubes [17]. There is a set of peaks in the range of 650-750 nm for SFM processed SWNTs that features presence of metallic nanotube transitions (M_{11}) [17].

1.2 Photoluminescence (PL) Spectra and Excitation-Emission Photoluminescence (EPL) Maps

The PL spectra and EPL maps complement the absorption analysis of the studied SWNT dispersions. In Figure 3a, PL spectra of small diameter SWNTs are featuring emission from E_{11} level, with US dispersed nanotubes having peak (1002 nm) redshifted (Δ = 5 nm) relative to maximum (997 nm) of SFM dispersed SWNTs, correlating with above discussed absorption results. Gaussian fitting for the spectra in Figure 3a, allowed us to determine more accurately half-width at half-maximum (HWHM) for the peaks featuring (6,5) chirality, being practically the same for US and SFM processed SWNTs (Gaussian fitting parameters are presented in the supplementary Figure S2 and Table S2), where EPL maps of small diameter SWNTs have practically the same spectral features (Figure S3). However differential EPL maps in Figure 3b,c (obtained as a difference of the peak-normalized PL spectra and the peak-normalized PL spectrum of the (6,5) chirality at λ_{EX} = 570 nm) show the PL signals of other chiralities apart from intensive (6,5) chirality emission. The differential EPL map of SFM processed SWNTs have a distinctive peak of (7,5) chirality at the excitation and emission wavelengths 657 nm and 1034 nm, respectively, as shown in Figure 3c. There is practically no signature of this (7,5) chirality emission in the US processed dispersions as shown in Figure 3b.

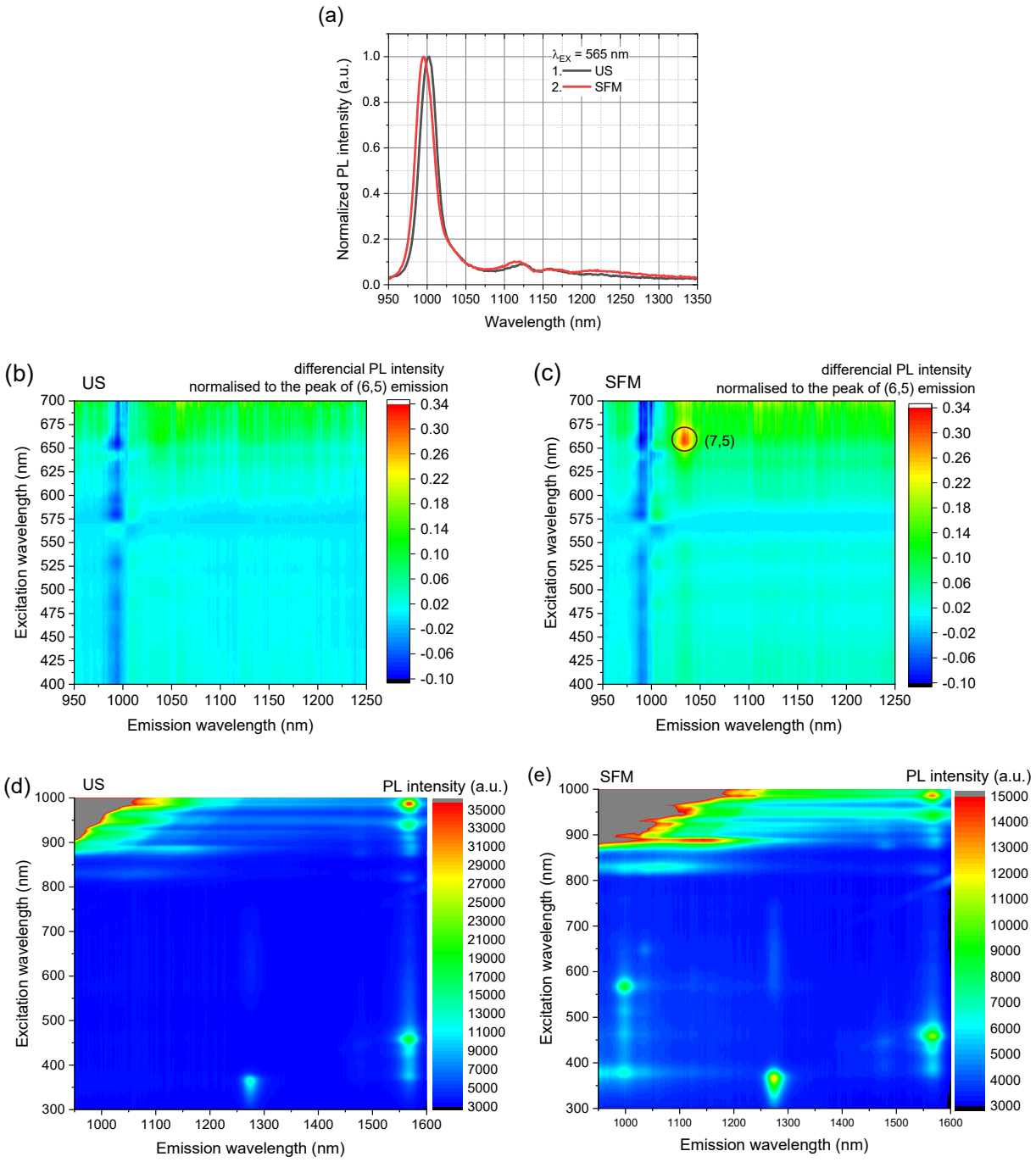


Fig. 3 (a) Normalized (for the maximum) photoluminescence (PL) spectra of small diameter SWNTs dispersed by US (curve 1) and SFM (curve 2) at the excitation wavelength 565 nm. (b,c) EPL maps of differential PL intensity (obtained as a difference of the peak normalized PL spectra and the peak normalized PL spectrum of the (6,5) chirality at the excitation wavelength of 570 nm) of small diameter SWNTs dispersed by US (b) and SFM (c). (d,e) EPL maps of large diameter SWNTs dispersed by US (d) and SFM (e)

The EPL maps of large diameter SWNTs (Figure 3d,e) evidence presence of multiple charities in such dispersions, confirming that the samples consist of a mixture of semiconducting nanotubes of varying diameters. The excitation–emission features extend across both near-IR and visible regions, characteristic of large diameter SWNTs (having smaller bandgaps). Distinct high-intensity peaks are observed at λ_{EX} = 986 nm and λ_{EM} = 1566 nm, that can be associated with (16,2) chirality (diameter of 1.35 nm) [16]. Another prominent band at λ_{EX} = 940 nm and λ_{EM} = 1566 nm is attributed to the (12,7) chirality (diameter of 1.32 nm). A relatively low intensity peak at λ_{EX} = 890 nm and λ_{EM} = 1573 nm can be associated to the (10,9) chirality. A peak at λ_{EX} = 368 nm and λ_{EM} = 1275 nm can be attributed to (11,1) chirality nanotubes (diameter 0.92 nm) [16]. A notable peak at λ_{EX} = 568 nm and λ_{EM} = 998 nm, corresponding to the (6,5) chirality, is evident in the SFM sample of large diameter SWNTs, but is absent in the US counterpart (Figure 3d,e). Such differences can be attributed to higher efficiency of dispersing nanotubes of various diameters by the SFM technique, and as result such dispersions have more varied by chiralities composition. An additional band at λ_{EX} = 458 nm and λ_{EM} = 1566 nm does not correspond to any established chirality from the Weisman et al (2003) database [16]. Therefore, one of the most reasonable justifications for this peak is energy transfer from the polymer (PFO-BPy) to the SWNT of (16,2) chirality.

1.3. Defect Analysis of SWNTs Using Raman Spectroscopy

Raman spectroscopy is considered as a valuable tool in assessment of SWNT quality and level of defects present on their surface. The Raman spectrum of carbon nanotubes typically includes the D-band in the range of 1300-1400 cm^{-1}, G-band in the range of 1500-1600 cm^{-1}), and G′ band (2D-band) around 2620-2650 cm^{-1}) [18]. For SWNTs, G-band consists of G^+ and G^- bands, where G^+ peak represents the carbon atom vibrations along the longitudinal axis of the nanotube (longitudinal optical phonon mode) and G^- peak is associated with the circumferential direction of vibration in the nanotubes (transverse optical phonon mode) [19]. For semiconducting SWNTs, the G^+ peak is typically much more intense than G^-. Among these, the D-band and 2D-band play critical roles in evaluating defect content [19].

Raman spectra normalized on G^+-band maximum of studied SWNT samples in the range of 1200 – 3000 cm^{-1} are summarized in Figure 4a. Spectral changes around D-, G- and 2D-bands are better evidenced in the Figure 4b showing the spectra in the narrower ranges of 1260-1650 and 2530-2730 cm^{-1}.

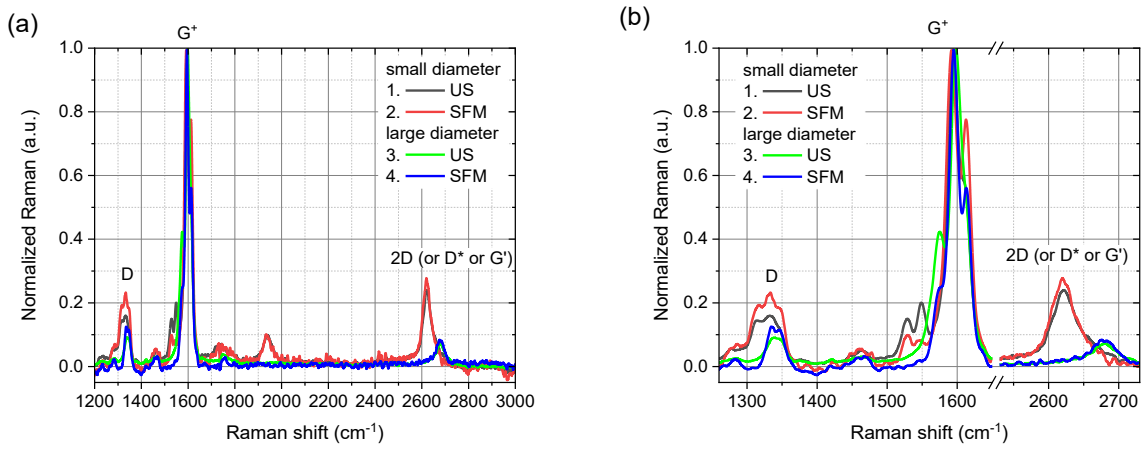


Fig. 4 Raman spectra of small-diameter SWNTs (curves 1 & 2) and large-diameter SWNTs (curves 3 & 4) dispersed by ultrasonication (US; curves 1 & 3) and shear-force mixing (SFM; curves 2 & 4). The spectra are shown over the ranges of 1200–3000 cm^{-1} (a), 1260–1650 cm^{-1}, and 2530–2730 cm^{-1} (b)

According to previous studies [14,18], the $2D/G^+$ intensity ratio is a most suitable way to estimate numerically the quality of the nanotubes. The commonly used D/G^+ ratio may be less reliable because it can be affected by the presence of nanotube bundles and other carbon materials. The intensity of each G^+ band has been evaluated by Lorentzian fitting of the spectra in the range of 1560-1650 cm^{-1}. Lorentzian fitting allows us to consider only G^+-band peaking at approx. 1594 cm^{-1} and to exclude the contribution of the sidebands around 1574 and 1614 cm^{-1}. The Lorentzian fitting parameters are provided in Supplementary Tables S3 and S4, with the corresponding fitted spectra shown in Supplementary Figure S4. The $2D/G^+$ ratio for each sample is presented in Table 2.

Table 2 The ratio of $2D/G^+$ with G^+ band intensity identified from Lorentzian fitting and values of G^+ HWHM (Table S4)

SWNT type	Processing method	$2D/G^+$ (intensity)	G^+ HWHM (b; cm^{-1})
small diameter	US	0.254	9.7
	SFM	0.297	9.1
large diameter	US	0.081	7.5
	SFM	0.087	7.5

For 2D peaks (intensity and area under the band), $2D/G^+$ ratios are consistently higher for SFM samples than US-treated. This result (higher $2D/G^+$ ratio) suggests that SFM better preserves the structure as well as optical quality of the SWNTs compared to US method. PLQY is a significant parameter for assessing optical quality, defect concentration, sample purity, and the effectiveness of SWNT processing techniques [20]. PLQY of the SWNTs decreases due to defects in their structure [21]. Therefore, a higher $2D/G^+$ ratio suggests that the nanotubes have

fewer defects and better light-emission properties. This is consistent with Kastner et al. who demonstrated a linear correlation between 2D/G^+ ratio and PLQY, and consequently level of defects (stronger sonication resulted in higher level of defects, lower PLQY and lower 2D/G+ ratio) [18]. Graf at al. have evidenced same pattern [14] as well as our results shown in Table 2.

Furthermore, Lorentzian fitting of G^+ peaks showed no change of HWHM for large diameter nanotubes (Table 2). However, small diameter SWNTs have wider HWHM for US treatment (9.7 cm^{-1}) compared to the SFM samples (9.1 cm^{-1}). These HWHM estimates give one more evidence of higher levels of Raman scattering for US processed nanotubes.

2. FET Characterization

Aiming to elucidate the possible impact of US and SFM on transport of charge carriers in small and large diameter SWNTs, FET-based current-voltage (I-V) characteristics were measured for same set of four samples studied in the preceding section. To ensure statistical reliability, at least 36 FETs for each sample were fabricated and characterized. Representative output and transfer I-V characteristics of the studied FETs are shown in Figure 5 to illustrate the typical device behavior. In output I-V characteristics, the source-drain current, I_{DS}, as a function of source-drain voltage, V_{DS}, at various fixed gate-source voltage, V_{GS}, are plotted (Figure 5a). The transfer characteristics have I_{DS} vs. V_{GS} at constant V_{DS} (Figure 5b). From I-V data, key transistor parameters such as the ratio of on/off current, charge carrier mobility, μ, threshold voltage (V_T) and subthreshold swing (SS) were extracted, enabling a detailed assessment of device switching performance and electrostatic control.

The on-off current ratio of resultant output current-voltage characteristics was above 10^3. Effective μ (extracted from transfer I-V characteristics [22] were in the range from 0.01 up to 0.1 (cm^2 V^{-1} s^{-1}). Low values of extracted mobility are attributed to randomized nanotube networks in the bottom-gate FET architecture (used due to its simplicity), non-optimized FET insulator/electrodes, and remnant polymer used for sorting. While individual SWNTs exhibit ballistic transport with high mobility, network charge transport is dominated by hopping mechanisms between nanotubes, often limited by junction resistance, transitioning from diffusive to more efficient (ballistic) transport in the on-state [23]. Average V_T and standard deviations, for V_T have been identified from transfer I-V curves and summarized for all four sets of the SWNT samples in Table 3. Observed variations of V_T (from – 13.2 to – 15.3 V) are within the evaluated standard deviation (Table 3), and any V_T differences cannot be associated with nanotube processing technique. Furthermore, subthreshold swing (SS) has been extracted for studied FETs; allowing us to calculate SS average and standard deviation, σ, for SS being summarized in Table 3. Average SS for US and SFM processed SWNTs are quite different and further analysis of this parameter allows us to estimate level of charge carrier traps in different samples.

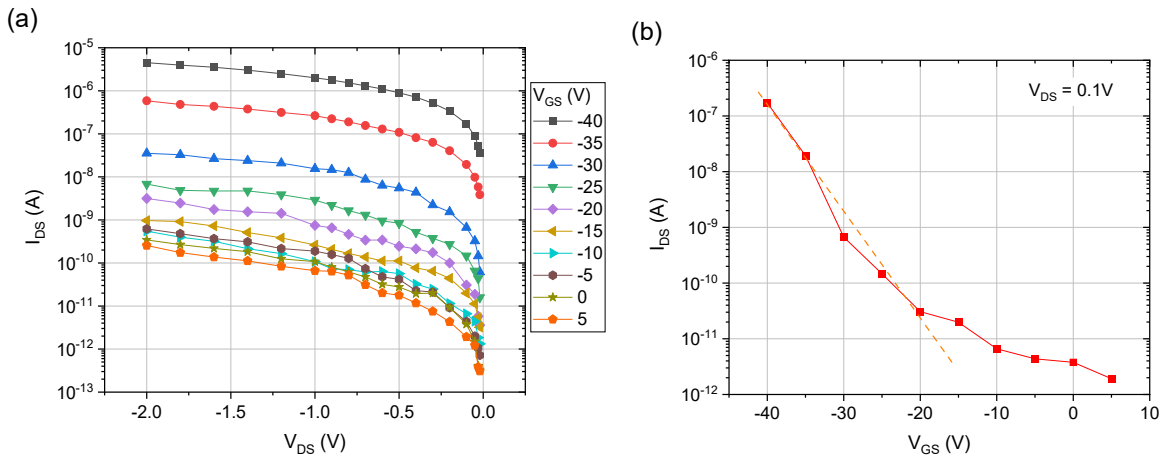


Fig. 5 Exemplary output (a) and transfer (b) current–voltage characteristics (at V_{DS} = 0.1 V) of the studied FETs; (a) output characteristics are shown for V_{GS} changing from – 40 V (very top) to +5 V (very bottom); (b) transfer characteristic is shown for V_{DS} = 0.1 V

Table 3. Average threshold voltage (V_T), standard deviation, σ, for V_T, sub-threshold swing (SS) standard deviation, σ, for SS, and interface trap density (D_{it})

SWNT type	Processing method	Average V_T (V)	σ for V_T (V)	average SS (V/decade)	σ for SS, (V/decade)	D_{it} (eV^{-1} cm^{-2})
small diameter	US	– 13.8	4.7	14.31	5.9	$5.72\ 10^{13}$
	SFM	– 15.3	4.2	7.53	2.2	$3.00\ 10^{13}$
large diameter	US	– 13.2	4.5	16.21	3.2	$6.49\ 10^{13}$
	SFM	– 13.5	7.7	4.87	2.4	$1.93\ 10^{13}$

In the sub-threshold region (where V_{GS} is below V_T), mobile charge carriers are not governed by equations (1), (2) [24]:

$$I_{DS,linear} = \frac{\mu W C_i}{L}(V_{GS} - V_T)V_{DS} \quad (1)$$

$$I_{DS,saturation} = \frac{\mu W C_i}{2L}(V_{GS} - V_T)^2 \quad (2)$$

where $I_{DS,linear}$ and $I_{DS,saturation}$ source-drain currents for linear and saturation regions, respectively; μ is charge carrier mobility, W and L are area width and length of the channel, C_i is surface capacitance of the insulator. Instead, the I_{DS} is limited by diffusion of charge carriers in the channel, and the diffusion process is controlled by the gradient of carrier concentration, where traps of charge carriers present in the channel and at the interface of semiconductor and

insulator have dramatic impact on I_{DS}. *SS* values are associated with interface trap density, D_{it}, via the following equations (3) and (4) [24].

$$SS = \frac{dV_{GS}}{d(log_{10}(I_{DS}))} = \frac{dV_{GS}}{d(\ln(I_{DS}))}\ln(10) = \frac{kT}{q}\ln(10)\left[1 + \frac{qD_{it}}{C_i}\right] \quad (3)$$

$$D_{it} = \frac{C_i}{q}\left[\frac{SS}{\ln(10)\frac{kT}{q}} - 1\right] \quad (4)$$

where k is Boltzmann constant, T is temperature {in K}, q stands for elementary charge. D_{it} characterizes quality of semiconductor material in the channel in terms of charge carrier trapping via formed defects and other imperfections [25].

Table 3 shows the values of D_{it} calculated using the formula (4). Just to note, D_{it} combines the traps in the bulk of the channel (SWNTs only) and at the interface of the channel and insulator, therefore some contribution of the traps from SiO_2 surface is present in these estimates. From Table 2, one can see that SFM processed SWNTs have lower level of traps density for both small and large diameter samples. This trend demonstrates that the US technique produces a greater number of interfacial trap states, likely due to structural disturbance, increased defect density, and residual contamination introduced during processing. Besides, this result correlates with spectral-related outcomes and literature data [13,14] on low density defects formed via SFM.

Moreover, the values of σ for *SS* are lower for SFM (2.2 and 2.4 {V/decade} – Table 2), indicating a more controlled interface and reduced defect-induced fluctuations. Thus, SFM method offers better reproducibility and device uniformity compared with US processing in subthreshold regions.

Overall, FET characterization results highlight that SFM not only enhances electrical performance but also significantly improves device-to-device consistency, making it the reliable fabrication method for SWNT-based FET applications. Although small diameter SWNT have better uniformity due to their chiral purity (having mostly nanotubes of (6,5) chirality) the large diameter SWNTs exhibit overall stronger transistor performance when all electrical parameters are considered together, which correlated with previous results [26].

Conclusion

A comparative analysis of four sets of SWNT samples (SFM and US processed for small and large diameter nanotubes) evidently demonstrates the superior device performance achieved using the SFM technique relative to conventional ultrasonication. Absorption and photoluminescent measurements, evidenced more red-shifted peaks for US processed SWNTs being associated with more defects present in such samples compared to SFM samples. Furthermore, SFM processing resulted in higher contributions of variable chiralities to the overall dispersions; for example, in small diameter nanotubes, higher contribution of (7,5) chiralities has been obtained, whereas (6,5) chirality emerged in large diameter SWNT dispersions. Raman spectra analysis, particularly the ratio of 2D/G^+ and HWHM, better quality SWNT are produced by SFM technique compared to ultrasonication processing.

FET characterization results confirm that the SFM method provides better electrical characteristics particularly in reducing the subthreshold swing and interface trap density compared with the ultrasonication approach. The consistently lower standard deviations observed in subthreshold swing further demonstrate the better reproducibility, stability, and uniformity achieved through SFM processing, making it highly effective for producing high-quality SWNT FETs suitable for advanced electronic applications. In particular, their lower subthreshold swing under SFM processing indicates more efficient channel switching and reduced trap-related scattering. The trap charge analysis also shows that the large diameter tubes contain fewer active trap states, resulting in better transport pathways and improved switching behavior.

References

1. S. Iijima, Nature 354, 56–58 (1991). https://doi.org/10.1038/354056a0
2. International Roadmap for Devices and Systems (IRDS™), 2024 Edition: Beyond CMOS Report (IEEE, 2024), https://irds.ieee.org/images/files/pdf/2024/2024IRDS_BC.pdf. Accessed 3 June 2026
3. M. F. L. De Volder, S. H. Tawfick, R. H. Baughman, A. J. Hart, Science 339, 535–539 (2013). https://doi.org/10.1126/science.1222453
4. P. Avouris, M. Freitag, V. Perebeinos, Nat. Photonics 2, 341–350 (2008). https://doi.org/10.1038/NPHOTON.2008.94
5. K. J. Hughes, K. A. Iyer, R. E. Bird, J. Ivanov, S. Banerjee, G. Georges, Q. A. Zhou, ACS Appl. Nano Mater. 7, 18695–18713 (2024). https://doi.org/10.1021/acsanm.4c02721
6. H.-Y. Liu, Y. Sun, D.-M. Sun, H.-M. Cheng, Adv. Funct. Mater. 35, 2424012 (2025). https://doi.org/10.1002/adfm.202424012
7. D. Goerzen, M. Pasquali, M. Kim, D. A. Heller, Nano Lett. 26, 4004–4013 (2026). https://doi.org/10.1021/acs.nanolett.5c05572
8. Y. Lin, Nat. Electron. 6, 506–515 (2023). https://doi.org/10.1038/s41928-023-00983-3
9. Y. J. Choi, E. J. C. Nacpil, J. Han, C. Zhu, I. S. Kim, I. Jeon, Adv. Energy Sustain. Res. 5, 2300219 (2024). https://doi.org/10.1002/aesr.202300219
10. M. H. Keshavarz, M. Fathi, Z. Shirazi, Fluid Phase Equilib. 599, 114534 (2026). https://doi.org/10.1016/j.fluid.2025.114534
11. X. Yu, A. Adronov, Small Methods 10, 2502086 (2026). https://doi.org/10.1002/smtd.202502086
12. M. M. R. Nayini, Z. Ranjbar, in Handbook of Carbon Nanotubes, ed. by J. Abraham, S. Thomas, N. Kalarikkal (Springer, Cham, 2022), pp. 341–392. https://doi.org/10.1007/978-3-030-91346-5_64
13. M. J. Shea, J. Wang, J. T. Flach, M. T. Zanni, M. S. Arnold, APL Mater. 6, 056104 (2018). https://doi.org/10.1063/1.5026853
14. A. Graf, Y. Zakharko, S. P. Schießl, C. Backes, M. Pfohl, B. S. Flavel, J. Zaumseil, Carbon 105, 593–599 (2016). https://doi.org/10.1016/j.carbon.2016.05.002
15. A. L. Ng, Y. Sun, L. Powell, C.-F. Sun, C.-F. Chen, C. S. Lee, Y. Wang, Small 11, 96–102 (2015). https://doi.org/10.1002/smll.201402118
16. R. B. Weisman, S. M. Bachilo, Nano Lett. 3, 1235–1238 (2003). https://doi.org/10.1021/nl034428i
17. K. S. Mistry, B. A. Larsen, J. L. Blackburn, ACS Nano 7, 2231–2239 (2013). https://doi.org/10.1021/nn305336x
18. M. Kastner, S. Stahl, I. Vollert, C. Loi, N. Rühl, T. Hertel, F. Schöppler, Chem. Phys. Lett. 635, 245–249 (2015). https://doi.org/10.1016/j.cplett.2015.06.076
19. A. C. Sparavigna, Carbon Nanotubes (Raman Spectroscopy), ChemRxiv (2024). https://doi.org/10.26434/chemrxiv-2024-xw377

20. T. Hertel, S. Himmelein, T. Ackermann, D. Stich, J. Crochet, ACS Nano 4, 7161–7168 (2010). https://doi.org/10.1021/nn101612b
21. M. Nirmal, L. Brus, Acc. Chem. Res. 32, 407–414 (1999). https://doi.org/10.1021/ar9700320
22. Y. Xu, Y. Li, S. Li, F. Balestra, G. Ghibaudo, W. Li, Y.-F. Lin, H. Sun, J. Wan, X. Wang, Y. Guo, Y. Shi, Y.-Y. Noh, Adv. Funct. Mater. 30, 1904508 (2020). https://doi.org/10.1002/adfm.201904508
23. J. Kim, Y. Oh, J. Shin, M. Yang, N. Shin, S. Shekhar, S. Hong, ACS Nano 16, 21626–21635 (2022). https://doi.org/10.1021/acsnano.2c10715
24. S. M. Sze, Y. Li, K. K. Ng, Physics of Semiconductor Devices, 4th Ed. (Wiley, Hoboken, NJ, 2021).
25. Y. Y. Illarionov, T. Knobloch, M. Jech, M. Lanza, D. Akinwande, M. I. Vexler, T. Mueller, M. C. Lemme, G. Fiori, F. Schwierz, T. Grasser, Nat. Commun. 11, 3385 (2020). https://doi.org/10.1038/s41467-020-16640-8
26. Y. C. Tseng, K. Phoa, D. Carlton, J. Bokor, Nano Lett. 6, 1364–1368 (2006). https://doi.org/10.1021/nl060305x

Statements and Declarations

Funding

P.L. acknowledges support from the Royal Society Research Grant (RGS\R2\192502).

Competing Interests

The authors have no competing interests to declare.

Author Contributions

All authors contributed to the study conception and design. Material preparation and data collection were performed by Debjani Goswami. Data interpretation, analysis, and drafting of the manuscript were performed by all authors. All authors read and approved the final manuscript.

Data availability

Data will be made available on request.

Supplementary Files

This is a list of supplementary files associated with this preprint. Click to download.

- SupplementaryInformation.pdf